Journal of Materials Chemistry A

ROYAL SOCIETY OF CHEMISTRY

PAPER

View Article Online
View Journal | View Issue

Cite this: J. Mater. Chem. A, 2024, 12, 8734

A "two-birds-one-stone" strategy to enhance capacitive deionization performance of flexible $Ti_3C_2T_x$ MXene film electrodes by surface modification†

Chuhan Huang,[ab] Tianqin Huang,[ab] Xue Liang Li,*[c] Wei Zhou[ab] and Meng Ding *[ab]

Two-dimensional transition metal carbides/nitrides (MXenes) have gained considerable prominence in capacitive deionization (CDI) due to their exceptional electrochemical activity and outstanding electronic conductivity. However, the further development of MXenes in practical applications in CDI is hampered by their limited narrow interlayer spacing and oxidation proneness. Herein, a dual-functional surface modification of $Ti_3C_2T_x$ MXene by sodium ascorbate (SA) is proposed to concurrently enhance the salt adsorption capacity and long-term stability. The modification by SA induces synergistic functions, including the enlargement of interlayer spacing, effective protection of Ti from oxidation, and exceptional electrical conductivity. Simultaneously, this film electrode is designed to be flexible and free-standing, devoid of binders or adhesives, showing promise for the large-scale production of CDI electrodes. Benefiting from these advantages, the SA-modified MXene exhibit excellent desalination performance, including high salt adsorption capacity (109.6 mg g^{-1}), high salt adsorption rates (17.5 mg g^{-1} min^{-1}), and impressive cycling stability (100% retention after 80 cycles). And the adsorption behavior of SA-modified MXenes is further investigated by *in situ* X-ray diffraction and density functional theory calculations. This work proposes an effective modification and explores theoretical aspects for fabricating MXene-based electrodes suitable for CDI and other electrochemical applications in moist or aqueous environments.

Received 11th January 2024
Accepted 27th February 2024

DOI: 10.1039/d4ta00236a

rsc.li/materials-a

1 Introduction

Capacitive deionization (CDI) is an emerging desalination technology, based on a reversible electrosorption process. The adsorption and desorption can be manipulated by adjusting external electrical potentials (≤2 V) across the two electrodes of CDI.[1–5] The inherent reversibility and comparatively low operational voltage bestow upon CDI a set of compelling attributes, encompassing high energy efficiency, cost-effectiveness in operation, and environmental friendliness.[6–8] The central constituents of CDI cells, electrode materials, stand as focal points in the advancement of CDI for practical applications.[9,10] A spectrum of functional nanomaterials, such as graphene,[11] activated carbon,[12] nitrogen/phosphorus-doped carbon,[13] reduced graphene oxide,[14] biomass-derived porous carbon,[15] yolk–shell carbon composites,[16] and metal–organic frameworks[9,10] finds widespread utilization as electrode materials in CDI devices.[17] However, most of these materials suffer from low desalination capacity (≤30 mg g^{-1}), high energy consumption, or complexity of production, which limit further development.[18,19]

Recently, a group of two-dimensional (2D) materials, MXenes, has demonstrated promising purification behavior of various organic and inorganic pollutants, which is ascribed to its incredible features, such as a tunable structure, excellent electrochemical properties, good hydrophilicity, and antimicrobial properties.[20–26] In CDI, the salt adsorption capacity of MXene-based electrode materials has reached over 70 mg g^{-1}, which is much higher than that of carbon-based electrodes.[27] But in practice, the fabrication and testing of MXene electrodes for long-term desalination are still challenging as MXenes are prone to self-stacking and oxidative degradation in an ambient environment.[28] The self-stacking during film formation is due to the electrostatic interactions between MXene nanosheets, which leads to a decrease in the surface active sites and sluggish ion transfer.[29] Moreover, MXenes are prone to oxidation and degradation when exposed to air and/or water, where the oxidation process generally starts at the edge position and subsequently extends towards the interior, eventually

[a]Department of Chemistry, School of Science, Xi'an Jiaotong-Liverpool University, Suzhou 215123, P. R. China. E-mail: Meng.Ding@xjtlu.edu.cn
[b]Department of Chemistry, University of Liverpool, Liverpool L69 7ZD, UK
[c]Pillar of Engineering Product Development, Singapore University of Technology and Design, 487372, Singapore. E-mail: xueliang_li@sutd.edu.sg

† Electronic supplementary information (ESI) available. See DOI: https://doi.org/10.1039/d4ta00236a

converting MXenes to TiO_2 within 15 days under ambient conditions.[30] The poor oxidation stability of $Ti_3C_2T_x$ MXene limits its long-term storage and practical applications. Thus, it is critical to design better protection of MXene-based electrodes for CDI and other applications in humid/aqueous environments.

To address the oxidation issue of MXene electrodes, considerable research efforts have been dedicated to the design of protective heterostructures for MXenes. For example, Natu *et al.* found that capping the edges of MXenes using polyphosphate salts increased the storage time of MXenes in aerated water by at least three weeks, which is a simple and effective way to enhance the antioxidant properties of MXenes.[31] Yang *et al.* prepared a three-dimensional (3D) $Ti_3C_2T_x$ MXene/graphene/carbon nanotube hybrid hydrogel using the gelation method for supercapacitor electrodes. The hybrid hydrogel demonstrated excellent oxidation resistance, and the electrical resistance of the material increased by only 9.3% after 60 days of storage under ambient conditions.[32] Li *et al.* synthesised GO/$Ti_3C_2T_x$ MXene/GO flexible freestanding films as electromagnetic interference (EMI) shielding materials with a stable performance for 70 days.[33] In the application of CDI, Cai *et al.* developed a 3D heterostructure MoS_2@MXene through a hydrothermal method. The MoS_2 nanosheets were vertically anchored on the MXene flakes *via* strong coordination to shield the oxygen from the surface of MXenes and this improved the electrochemical stability, which led to excellent salt removal capacity (35.6 mg g^{-1}).[34] However, it is still challenging to avoid the reaction of MXenes with dissolved oxygen and H_2O molecules in an aqueous solvent during the hydrothermal synthesis. Hence, Zhang *et al.* designed a synthesis route of covalent organic framework (COF)-on-MXene heterostructures in organic solvent, which alleviated the oxidative degradation caused by H_2O molecules. By engineering the inorganic–organic heterointerface, the uniform COF coating endowed the inner MXene with excellent oxidation resistance and sodium ion adsorbability (53.1 mg g^{-1}) in CDI.[35]

While advanced strategies have been proposed to mitigate MXene oxidation in the context of CDI electrodes, their practical implementation remains challenging. This challenge arises from intricate fabrication processes that unavoidably escalate production costs and carbon emissions. To support carbon neutrality goals, we propose a simple yet effective preparation method of oxidation stable $Ti_3C_2T_x$ MXene electrodes by edge capping of sodium ascorbate (SA) on MXenes, which enhances their oxidation resistance in aqueous solution while retaining their advantages in CDI. SA is a preservative with low cost and environmental benignity, and is widely used in the food and pharmaceutical industries.[36] The ascorbate acid ions can act as a capping and anti-oxidizing agent,[37] and can interact with oxygen-containing functional groups on the surface of MXenes to form hydrogen bonds and Ti atoms in MXenes to form coordination bonds. Since most of the oxidation of MXenes starts from their edges and surface functional groups,[31,38] capping of MXenes by ascorbate ions is considered to be effective in enhancing their antioxidant properties. Sodium ions can intercalate within MXene nanosheets, expanding the interlayer spacing and thereby enhancing the CDI performance.[39] Furthermore, the SA modification preserves the functional groups affixed to the MXene surface, thereby maintaining the structural integrity and intrinsic benefits of these functional groups. The advantages include enhanced electrochemical activity and improved salt absorption.[40] SA-MXene materials can be prepared as flexible membrane electrodes by vacuum filtration, which ensures a uniform thickness of the membrane structure. Since the addition of a conductive agent and a binder is not required, it does not suffer from the negative effects on the ion transport performance caused by them.[41] Moreover, due to the flexibility of the membrane material, it has the potential to be used in irregularly shaped CDI batteries. The synergistic effect endows SA-modified MXene with excellent oxidation resistance (stable storage for 90 days under ambient conditions) and promising CDI performance with a high salt adsorption capacity of 109.6 mg g^{-1}, fast average salt adsorption rate (17.5 mg g^{-1} min^{-1}), and long-term stability (80 cycles with 100% retention). The mechanism of sodium ion adsorption/desorption processes is investigated *via in situ* X-ray diffraction (XRD) and density functional theory (DFT) calculations. This work is expected to develop the MXene-based composites with excellent oxidation stability and reduced carbon-footprint fabrication for applications in aqueous or humid environments.

2 Results and discussion

The schematic synthesis process of SA-MXene is illustrated in Fig. 1a. Pristine $Ti_3C_2T_x$ MXene nanosheets were prepared from the Ti_3AlC_2 MAX by etching with LiF and hydrochloric acid at 35 °C for 24 hours, followed by ultrasonication in an argon stream for 30 minutes. Then, the pristine MXene colloidal suspension was modified by aqueous SA solution with different concentrations (8, 12, and 16 M) to obtain SA-MXene with SA to MXene ratios of 10.9 wt%, 16.4 wt%, and 21.8 wt%, respectively. The ascorbate ions coordinated the Ti atoms effectively *via* Ti–O bonds, forming a uniform protective layer on the surface of MXene nanosheets. Moreover, the ascorbate ions worked with the sodium ions to enlarge the interlayer spacing for faster ion migration. The SA-MXene was collected by vacuum-assisted filtration to obtain flexible and free-standing electrodes with a diameter of around 4 cm (Fig. 1b). The interlayer spacing of SA-MXene is large enough (4.2 Å, determined by XRD results) to support both sodium (1.84 Å Stoke radius) and chloride hydrate ion (1.81 Å Stoke radius) adsorption in a membrane CDI device (Fig. 1c).[42]

The surface morphology and material structure of the pristine MXene sample were studied by transmission electron microscopy (TEM). Fig. 2a shows a piece of a thin MXene nanosheet with an average lateral size of approximately 735 ± 19 nm. Fig. 2b and c present the high-resolution TEM (HR-TEM) image and selected area electron diffraction (SAED) pattern, respectively. In the diffraction pattern of MXenes, multiple bright rings can be observed, which represent the (002), (004), (006), and (008) lattice planes from the inside to the outside, respectively. These observed lattice planes demonstrate the appearance of MXene crystals. The HR-TEM image (Fig. 2c) with

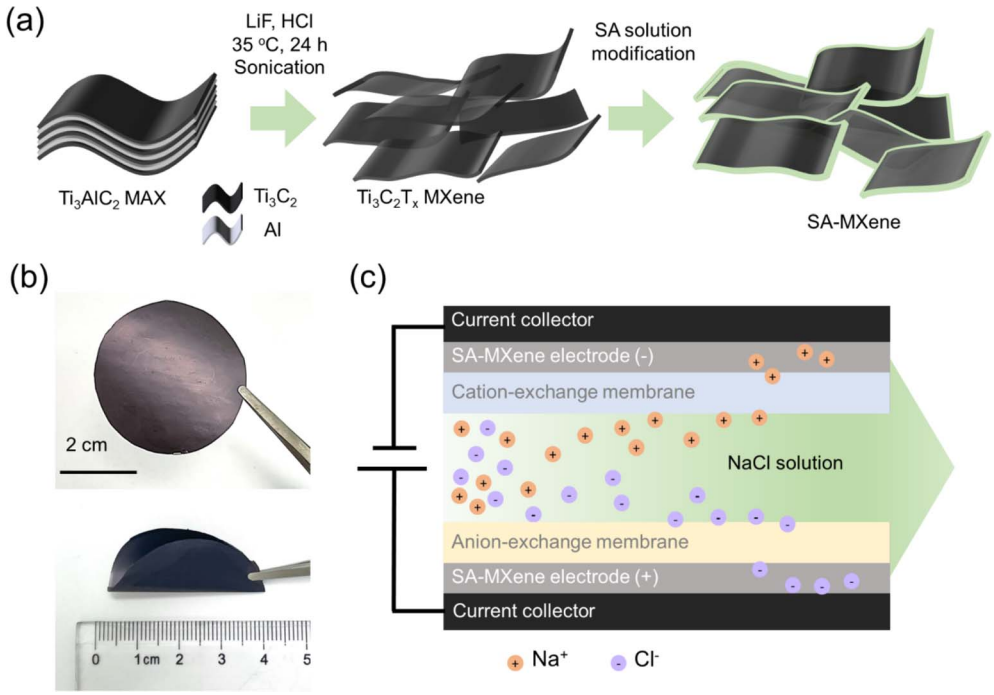

Fig. 1 (a) Schematic illustration of the preparation process of pristine MXenes and SA-MXene. (b) Digital images of an SA-MXene electrode. (c) Schematic illustration of the MCDI configuration with SA-MXene electrodes.

the fast Fourier transform (FFT) pattern indicates that the lattice fringes in MXenes are 0.80 nm, which correspond to the typical (002) lattice plane. These lattice planes can be attributed to the crystalline structure of MXenes, which provides evidence that high purity MXenes were successfully synthesized.[43,44]

The crystal structure and composition of the samples were studied by XRD (Fig. 2d). A distinct sharp peak at 2θ angle = 6.8° can be observed in the XRD pattern of MXenes, which represents the (002) lattice plane and well aligns with the HR-TEM results.[45] The peak representing the (002) lattice plane should also be observed in the other three SA-MXene samples due to the presence of MXenes. However, the 2θ angles shift to a slightly smaller value (5.6°). This indicates the delamination of SA-MXene and the expansion of the interlayer spacing of the SA-MXene (4.2 to 7.0 Å). This is due to the insertion of Na ions in the MXene interlayers and the coordination effect between SA and Ti atoms.[46,47] The Stokes radius of sodium ions in water is 1.84 Å,[48] and the layer spacing of MXenes prepared in this study is 4.2 Å. Therefore, MXenes can provide enough space for sodium ions to be embedded, and the sodium ions will be spontaneously intercalated into MXenes in the hydrated state by electrostatic attraction.[49] Notably, the expansion by sodium ions and ascorbate ions is reversible if treated with HCl (Fig. S1a†), suggesting that the expansion and coordination wouldn't lead to structural distortion or damage. The schematic illustration of SA-MXene is shown in Fig. S1b,† demonstrating the increased spacing of MXene layers by coordination with ascorbate ions through Ti–O bonding. The increased interlayer spacing is expected to improve CDI performance by facilitating the diffusion of the ions and providing more ion-accessible adsorption sites, which will increase the storage capacity of ions.[39] The Fourier transform infrared (FTIR) spectra of pristine MXenes, SA-MXene, and SA are displayed in Fig. S2.† Compared with pristine MXenes, SA-MXene presents stretching bands at 1756 (C=O of the five-membered lactone ring), 1675 (C=C of the five-membered lactone ring), 1320 (C=C), and 1027 (C–O–C) cm^{-1}, which are characteristic bands of SA. Notably, the C=C band in SA-MXene shifts towards a lower value compared to that of SA (1322 cm^{-1}) as a result of the interaction of ascorbate ions with Ti in MXenes.[50,51]

The chemical bonding of functional groups present on the surface of the sample was investigated using X-ray photoelectron spectroscopy (XPS). Fig. 2e shows the XPS survey spectra of MXenes and 12-SA-MXene. The XPS survey spectra of 8-SA-MXene and 16-SA-MXene are presented in Fig. S3 and S4.† It can be observed that the peaks in the XPS survey spectra of MXenes and SA-MXene are essentially identical, both containing C 1s, Ti 2p, O 1s, and F 1s peaks.[52] Notably, a distinct Na 1s peak (~1080 eV) can only be observed in the spectrum of SA-MXene due to the modification by SA. The C 1s XPS spectrum of pristine MXenes is shown in Fig. 2f. This spectrum contains four peaks at 281.7, 283.5, 284.8, and 286.1 eV, respectively. Among them, the peaks at 281.7 and 284.8 eV represent the Ti–C and C–C bonds, respectively, which are from the $Ti_3C_2T_x$ MXene. The presence of peaks at 283.5 and 286.1 eV indicates the bonds of Ti–C–O and C–O, which come from the –OH on the surface of MXene nanosheets.[53] In contrast to the spectrum of pristine MXenes, the spectrum of SA-MXene (Fig. 2g) is composed of five peaks at 281.7, 283.5, 284.8, 286.1, and 288.4 eV, respectively. Among them, the first four peaks are in the same positions as in the MXene spectrum and represent the same chemical bonds. However, the last peak at 288.4 eV

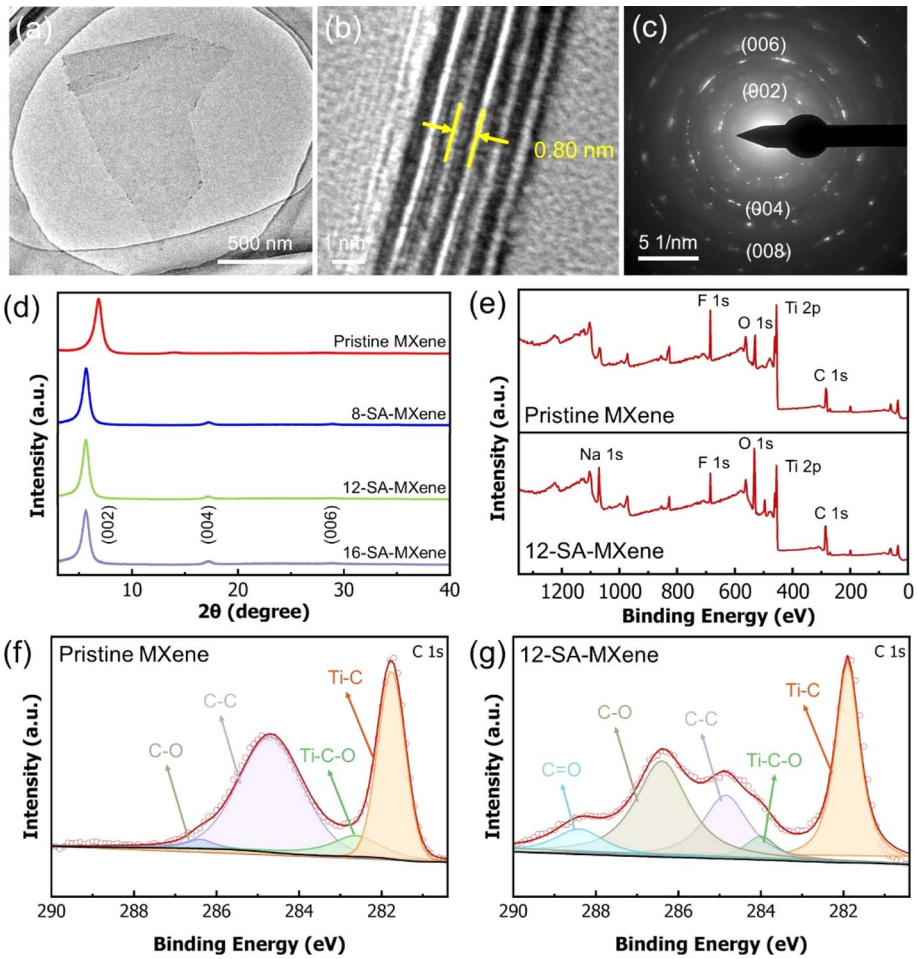

Fig. 2 (a) TEM image, (b) HR-TEM image, and (c) SAED pattern of pristine MXenes. (d) XRD patterns of pristine MXenes, 8-SA-MXene, 12-SA-MXene and 16-SA-MXene. (e) XPS survey spectrum of pristine MXenes and 12-SA-MXene. High resolution XPS spectra of the C 1s region of (f) pristine MXenes and (g) 12-SA-MXene, respectively.

represents the C=O bond, which is not usually present in Ti_3C_2 MXene. Instead, this peak represents the C=O bond in ascorbate ions, suggesting the successful binding between ascorbate ions and MXenes.[54] The results of TEM, XRD, and XPS indicate that high-purity $Ti_3C_2T_x$ MXene and SA-MXene were successfully synthesized by the previous steps.

The oxidation stability of SA-MXene was investigated by comparing the appearance, nanostructure, and optical properties of freshly prepared samples, and those stored under ambient conditions for 90 days were assessed using a combination of qualitative and quantitative methods. First, the degree of oxidation of different materials can be qualitatively analyzed by using their visible appearance, XRD, and TEM images. Fig. 3a shows the color difference between fresh MXenes and different MXene samples of the same initial concentration after 90 days of storage, which implies the different oxidation stages. Fig. 3a(i) and (ii) exhibit the photographs of fresh MXenes and pristine MXene samples after 90 days of storage, respectively. It is obvious that the fresh MXene dispersion appears dark green, while a pristine MXene dispersion after 90 days of storage changed from dark green to off-white, which is due to the oxidation and degradation of MXenes in solution where most of the MXene nanosheets have oxidatively degraded and changed to white-colored TiO_2. Fig. 3a(iii–v) show 8-SA-MXene, 12-SA-MXene, and 16-SA-MXene solutions after 90 days of storage, respectively. The color of the three SA-MXene solutions after 90 days of storage still appeared dark green, which indicates that the oxidative degradation of MXenes was effectively restricted by SA. Additionally, TEM was employed to observe the surface morphology of various samples after long-term storage. TEM images of MXene and SA-MXene series (Fig. 3b) demonstrate their 2D nanosheet structures. However, there are a significant number of black needle-like TiO_2 crystals around the edges of MXene sheets, resulting in a severely damaged structure. In contrast, TEM images of the other three SA-MXene samples show neat and intact sheet structures without the presence of numerous black crystals. This is further proved by the XRD pattern comparison of SA-MXene and pristine MXenes after 90 days of storage (Fig. S5†), in which the SA-MXene retains the original $Ti_3C_2T_x$ (002) peak while the pristine only presents feature peaks of anatase-rutile TiO_2 at 25.3° (101) and 27.3° (110).

To further investigate the oxidation resistance differences quantitatively between these three samples, UV-vis spectroscopy

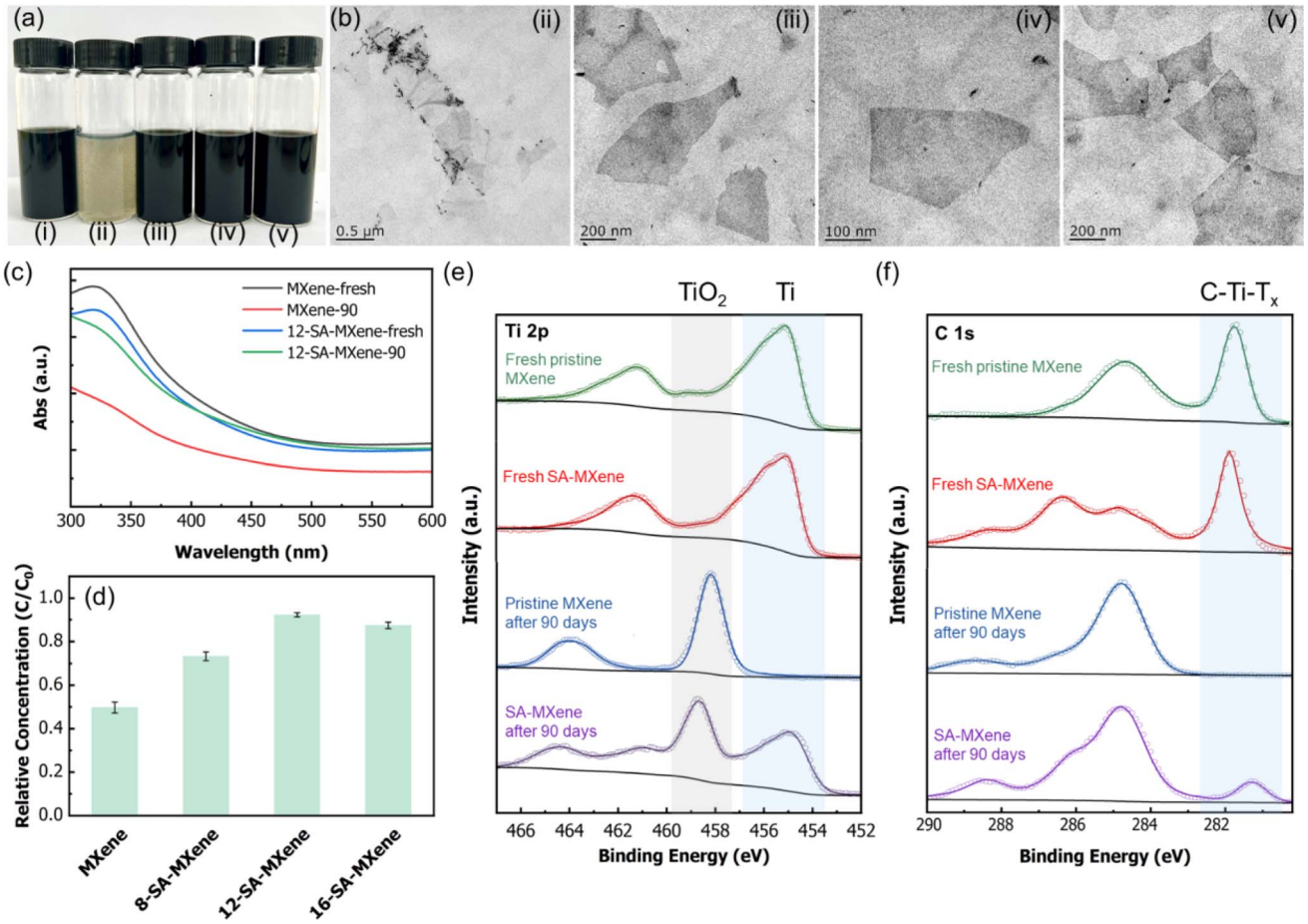

Fig. 3 (a) Digital photograph and (b) TEM images of (i) fresh MXenes, (ii) MXene, (iii) 8-SA-MXene, (iv) 12-SA-MXene and (v) 16-SA-MXene after 90 days of storage. (c) UV-vis spectrum and (d) relative concentration (C/C_0) of fresh pristine MXenes, pristine MXenes after 90 days of storage, fresh 12-SA-MXene, and 12-SA-MXene after 90 days of storage. High-resolution XPS spectrum comparison of (e) Ti 2p and (f) C 1s for fresh and stored MXene samples.

was applied to measure the changes in their optical properties. UV-vis spectra (Fig. 3c and S6†) compared MXene samples before and after 90 days of storage. Fig. 3c shows the UV-vis spectra of fresh pristine MXenes (MXene-fresh) and after storage (MXene-90), fresh MXene modified with 12 mM SA (12-SA-MXene-fresh) and after storage (12-SA-MXene-90). According to the Beer–Lambert law, the absorption (Abs) of the same substance under the same conditions is proportional to the concentration of the substance.[55] The UV-vis spectra show that after 90 days of storage, there was only a small decrease in the absorption peak intensity of 12-SA-MXene, suggesting a restricted degradation in the 12-SA-MXene solution, which is much lower than that of the unmodified MXene solution. The relative concentrations of MXenes in all samples, *i.e.*, the ratio of MXene concentration after 90 days of storage to MXene concentration in fresh solution, are calculated by using the Beer–Lambert law and compared in Fig. 3d. Amongst the three SA-MXene samples, 12-SA-MXene has the highest relative concentration of 0.92, indicating the most outstanding anti-oxidation ability. The relative concentrations of 8-SA-MXene and 16-SA-MXene are 0.73 and 0.87, respectively.

For the antioxidant capacity of SA-MXene, both the content of ascorbate acid ions and the pH of the dispersion play a crucial role. For 8-SA-MXene, since the amount of ascorbic acid ions is low, they may not be able to completely protect MXenes from edge capping and shielding, resulting in it being more susceptible to oxidation. In the three samples, the pH of the 16-SA-MXene dispersion was 3.68, which was higher than that of 8-SA-MXene (3.48) and 12-SA-MXene (3.56). Due to the increase in hydroxide ion content in the solution, the negatively charged OH^- ions will combine with the positively charged MXene edges and accelerate its oxidation process. The excess hydroxide ions can also cause the conversion of –OH groups on the surface of MXenes into $–O^-$ *via* a 56 reaction. The $–O^-$ groups may increase the surface activity of MXenes and reduce their stability to some extent.[56] For the 12-SA-MXene sample, the ascorbic acid ion content in the dispersion is higher than that of 8-SA-MXene, allowing for better edge capping and shielding. Compared to 16-SA-MXene, 12-SA-MXene has a smaller pH value. As a result, the extent of the adverse effects on 12-SA-MXene caused by hydroxide ions is low, giving it optimal anti-oxidant ability.

The chemical composition of fresh and stored MXenes was investigated by XPS (Fig. S7, S8 and Table S1†). The high-resolution spectra of Ti 2p and C 1 s in the as-prepared and stored MXenes are displayed in Fig. 3e and f, respectively. In the Ti 2p spectra (Fig. S8†), there are five deconvoluted peaks at 454.9, 455.9, 457.1, 458.5, and 459.3 eV, representing Ti^{+}, Ti^{2+}, Ti^{3+}, and Ti^{4+}, respectively. And C 1s spectra were deconvoluted into Ti–C, Ti–C–O, C–C, and C–O. In Table S2,† it is shown that the percentage of Ti content in fresh SA-MXene with low oxidation states (+2 and +3) increases compared with that in pristine MXenes, which is ascribed to the Ti reduction by SA coordination. During the oxidation processes, Ti^{+} is oxidized to Ti^{2+} and Ti^{3+}, and eventually to Ti^{4+}.[36] As presented in Fig. 3e and f, the intensities of Ti^{+} (Ti–C and Ti–F), Ti^{2+}, and Ti^{3+} peaks decreased and the C–Ti–T_x peak in pristine $Ti_3C_2T_x$ MXene disappeared after 90 days of storage, yet the peak of Ti^{4+} (TiO_2) increased obviously, suggesting severe oxidation of pristine MXenes. As for 12-SA-MXene, the peak intensities of Ti^{+}, Ti^{2+}, Ti^{3+}, and C–Ti–T_x reduced after 90 days of storage yet remain, indicating adequate protection of $Ti_3C_2T_x$ MXene by SA from severe oxidation under ambient conditions. Therefore, it can be concluded that unmodified MXenes were severely oxidized after 90 days of storage, whereas SA-modified MXene, especially 12-SA-MXene, still showed impressive stability even after 90 days.

As the principle of CDI is based on electrochemical adsorption, it is important to investigate the electrochemical properties of electrodes and select the most suitable electrode material for use in CDI cells. In this report, cyclic voltammetry (CV) and electrochemical impedance spectroscopy (EIS) are utilized to analyze the electrochemical performance of the MXene and SA-MXene series.[57] Fig. S9a and b† show the CV curves of fresh MXenes and MXenes stored for 90 days at various scan rates, respectively. After 90 days of storage, the electrochemical performance of MXenes deteriorates due to severe oxidation (Fig. S9c†). At a scan rate of 5 mV s^{-1}, the specific capacitance of the aged MXene is only 28.4 F g^{-1}, which is 33.1% that of the fresh MXene. However, the SA-MXene demonstrates improved electrochemical performance compared to the aged MXene. Fig. 4a displays the CV patterns of the three SA-MXene samples at a scan rate of 50 mV s^{-1}. The CV curves for all samples show a typical sub-rectangular shape similar to that of the fresh MXene electrode.[58] The area enclosed by the CV curve of 8-SA-MXene is the largest compared to that of 12-SA-MXene and 16-SA-MXene, indicating that the specific capacitance of 8-SA-MXene is the highest amongst the three samples. This is probably because this sample is modified using the lowest concentration of SA, which has the least effect on the electrical conductivity and the functional groups attached to the MXene surface.[40] The CV curves of 8-SA-MXene and 16-SA-MXene are presented in Fig. S10 and S11.† The CV curves of 12-SA-MXene at different scan rates have similar shapes without obvious distortion (Fig. 4), indicating an excellent rate performance. The specific capacitances of 8-SA-MXene, 12-SA-MXene and 16-SA-MXene at various scan rates in a 1 M NaCl aqueous solution are shown in Fig. 4c. Among all the samples, the 8-SA-MXene shows the highest specific capacitance at a scan rate of 5 mV s^{-1} (58.77 F g^{-1}), which is higher than that of the 12-SA-MXene (47.42 F g^{-1}) and 16-SA-MXene (41.43 F g^{-1}). For 16-SA-MXene, the content of MXenes in this sample is relatively low (58.1%). Considering that the specific capacitance is mainly contributed by the MXene nanosheets, the lower content of MXenes would lead to a decrease in the specific capacitance.

EIS was applied to measure the internal resistance and electrical conductivity of different samples. Fig. 4d shows the

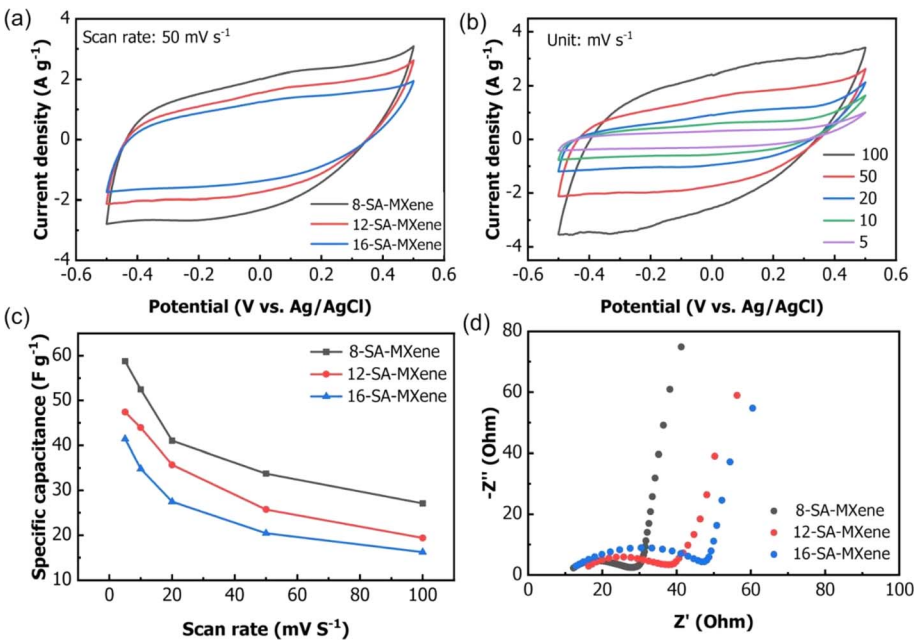

Fig. 4 (a) CV curves of 8-SA-MXene, 12-SA-MXene and 16-SA-MXene with a scan rate of 50 mV s^{-1}. (b) CV curves for 12-SA-MXene with scan rates varied from 5 mV s^{-1} to 100 mV s^{-1}. (c) Specific capacitance comparison of 8-SA-MXene, 12-SA-MXene, and 16-SA-MXene at a scan rate from 5 mV s^{-1} to 100 mV s^{-1}. (d) Nyquist plots for 8-SA-MXene, 12-SA-MXene, and 16-SA-MXene.

Nyquist plots for 8-SA-MXene, 12-SA-MXene, and 16-SA-MXene. It can be observed that the EIS patterns of all samples consist of a semicircle in the high frequency region and a linear pattern in the low frequency region. The diameter of the semicircle can reflect the electron transfer characteristics of the sample between the interface of NaCl solution and electrodes.[59] It can be seen from the Nyquist plots that these three samples have relatively large electrical conductivity. A comparison of the diameters of the semicircles in the high frequency region reveals that the 8-SA-MXene EIS pattern shows the smallest diameter of the semicircle, while the 16-SA-MXene shows the largest diameter of the semicircle. This indicates that the polarization resistance of the samples increases with increasing concentration of SA modified MXenes. Among the three samples, 8-SA-MXene shows superior electrical conductivity, while 16-SA-MXene shows the least. The reason for the regularity of this variation may be the same as the reason that causes the variation of the specific capacitance. It can be noted from Fig. S12† that the diameter of the semicircle in the high-frequency region of the Nyquist plot of pure MXenes is smaller than that of SA-MXene, which indicates that pure MXenes possess the smallest resistance. Therefore, it can be understood that the electrical conductivity of the samples is mainly supported by the MXene nanosheets, and the concentration of MXene nanosheets is relatively the highest in 8-SA-MXene (73.8%), thus providing the material with excellent electrical conductivity.

To investigate the adsorption capacity and stability of electrodes prepared from SA-modified MXene nanosheets in CDI applications, several sets of tests were carried out in NaCl

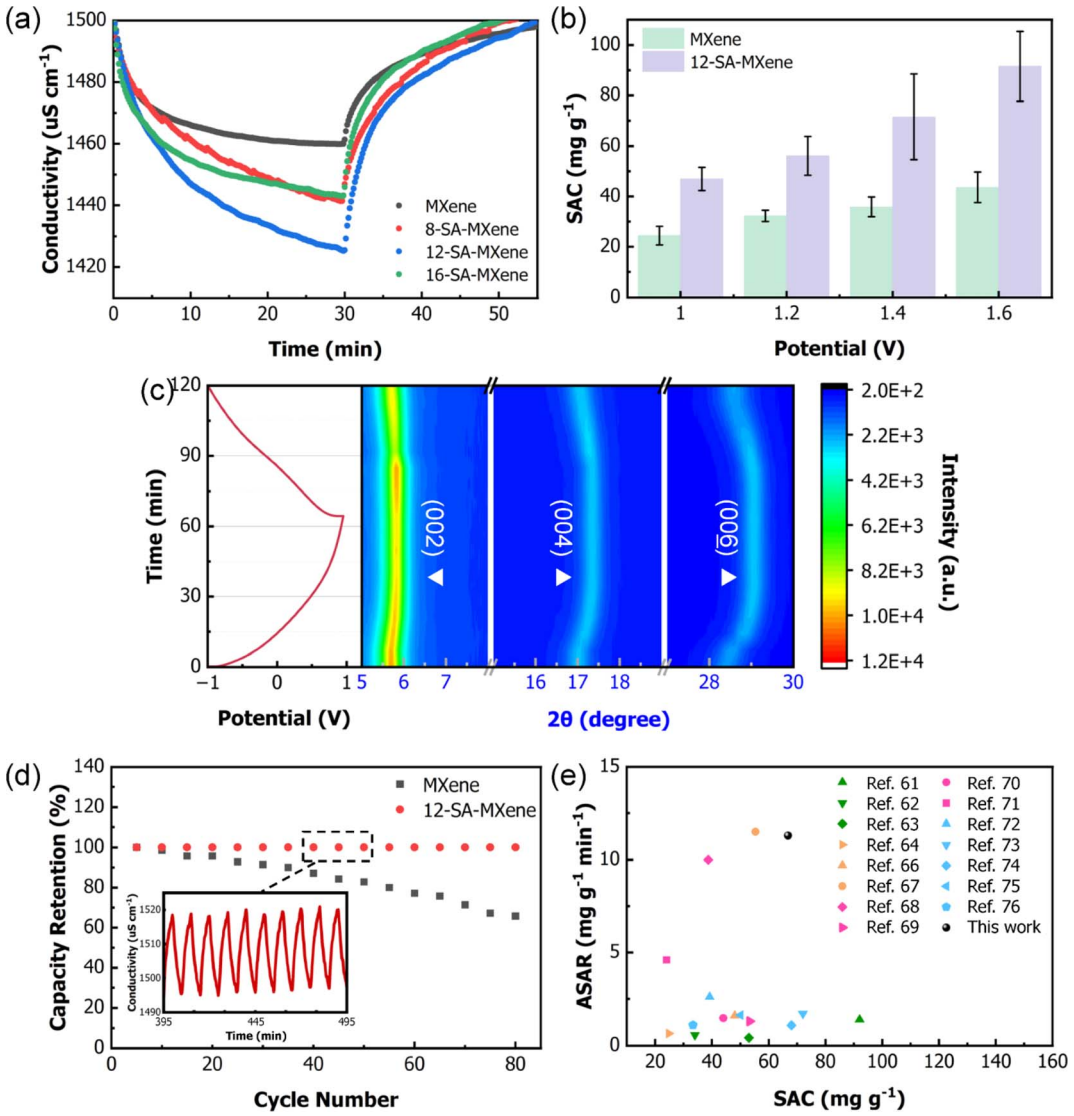

Fig. 5 (a) Plots of the change in solution conductivity with time corresponding to MXenes, 8-SA-MXene, 12-SA-MXene and 16-SA-MXene. (b) Specific SAC values of MXenes and 12-SA-MXene at different applied potentials. (c) Two-dimensional view of the *in situ* XRD result for intercalation into SA-MXene during charging and discharging from 2θ 5° to 30° (right) and the corresponding galvanostatic profile of SA-MXene at 15 mA g^{-1} (left). (d) CDI cycling performance of MXene and 12-SA-MXene electrodes. The inset shows the conductivity change of 12-SA-MXene during the 40–50th cycles. (e) CDI Ragone plot of 12-SA-MXene and samples from the literature.

solution with various concentrations. The CDI cells used in the test apparatus were homemade cells with the same electrode material for both the cathode and the anode. In this system, the NaCl solution was used as the feed solution, in order to determine the variation in salt adsorption capacity (SAC) of the same electrodes under different conditions. The concentration of the NaCl feed solution was varied from 250 mg L^{-1} to 750 mg L^{-1} in increments of 250 mg L^{-1}. In addition, the constant voltage applied to the cathode and anode of the CDI cell varied from $\pm$1 V to $\pm$1.6 V in unit of 0.2 V. The corresponding current responses of CDI electrodes are depicted in Fig. S13.† The changes in solution conductivity with time corresponding to different SA-MXene samples at an applied voltage of $\pm$1.4 V and a NaCl feed solution concentration of 750 mg L^{-1} are plotted in Fig. 5a. All SA-MXene electrodes have better desalination performance than the pristine MXene, due to the sufficient ion adsorption sites and faster ion transportation. It is noteworthy that the difference in salt adsorption behaviours between 8-SA-MXene and 16-SA-MXene is very slight, while the salt adsorption capacity of 12-SA-MXene is much higher than that of 8-SA-MXene and 16-SA-MXene. However, 8-SA-MXene exhibits the best electrochemical performance. The difference can be explained by the improved oxidation resistance of 12-SA-MXene with sufficient specific capacity. Compared with electrochemical tests, the CDI electrodes endure the stronger impact of water flowing through the cells, a higher charging/discharging potential range (up to $\pm$1.6 V), and a much longer testing duration (could be 1–2 weeks).[34] Hence, both antioxidant and electrochemical properties contribute to the enhanced desalination performance, synergistically.[60] Amongst the prepared samples, 12-SA-MXene has the best antioxidant ability based on the UV-vis spectral analysis, which benefits the long-term desalination performance. 8-SA-MXene has be highest specific capacitance and poor oxidation resistance, resulting in a significant drop in SAC. For 16-SA-MXene, the inferior SAC could be attributed to poor conductivity and lower specific capacity, consistent with the electrochemical test results.

Fig. S14† and 5b show the specific SAC values for MXenes and 12-SA-MXene in different initial concentration solutions and at different applied voltages, respectively. The SAC of both electrodes increases as the applied voltage or NaCl concentration increases. This illustrates that both the concentration of the feed solution and the voltage applied to the CDI cell affect the SAC of the CDI electrode. And 12-SA-MXene demonstrated superior SAC to pristine MXene under all conditions; the SAC of 12-SA-MXene reaches a maximum value when the applied voltage is $\pm$1.6 V and the concentration of the NaCl feed solution is 750 mg L^{-1} (109.1 mg g^{-1}). In contrast, the SAC of MXenes under the same conditions is 54.3 mg g^{-1}, only almost half the SAC of 12-SA-MXene.

To further confirm the crystal structure evolution during the Na^+ adsorption/desorption processes, *in situ* XRD experiments

Table 1 Electrochemical and CDI performance of MXene-based electrodes

Electrode materials	Voltage (V)	Solution (mg L^{-1} NaCl)	Specific capacitance (F g^{-1})	ASAR (mg g^{-1} min^{-1})	SAC (mg g^{-1})	References
MXene/polymer						
Covalent organic frameworks@MXene	1.6	1000	—	12.5	53.1	61
Cellulose fibers/MXene	1.2	600	14 280 at 10 mV s^{-1}	0.57	34	62
Polyvinyl alcohol/MXene	1.4	450	—	0.424	53	63
MXene/carbon						
MXene/carbon dots	1.2	86.4	144.4 at 20 mA g^{-1}	0.65 at 20 mA g^{-1}	24.8	64
MXene/carbon nanotubes	1.2	1168.8	123 at 0.1 A g^{-1}	—	12 $\pm$ 1	65
MXene/reduced graphene oxide	1.6	143.5	98 at 10 A g^{-1}	1.6	48	66
N,P-doped graphitic carbon/MXene	1.6	1000	90 at 0.5 A g^{-1}	11.5	55.3	67
MXene/metal composites						
Ni,Co-PBA@MXene/PPy	1.2	500	260 at 5 mV s^{-1}	10	38.7	68
TiO_2/Ti_3C_2	1.2	500	207 at 10 mV s^{-1}	1.3	53.3	69
$Fe_3O_4@Ti_3C_2T_x$	1.2	500	150 at 2 mV s^{-1}	1.47	44	70
MoS_2/MXene	1.2	500	145 at 2 mV s^{-1}	4.6	23.98	71
Pristine MXene						
S-$Ti_3C_2T_x$/L-$Ti_3C_2T_x$	1.2	1100	300 F cm^{-1} at 5 mV s^{-1}	2.61	39.18 $\pm$ 1.73	72
S-$Ti_3C_2T_x$/L-$Ti_3C_2T_x$	1.6	584.4	169 at 5 mV s^{-1}	1.7	72	73
LiF/HCL-etching MXene	1.2	585	127.76 at 100 mA g^{-1}	1.09	68 at 20 mA g^{-1}	74
Alk-$Ti_3C_2T_x$-MXene	1.2	58 440	95.6 at 100 mV s^{-1}	1.63	50 $\pm$ 3 at 30 mA g^{-1}	75
Mg^{2+}-MXene aerogel	1.4	1000	—	1.1	33.3	76
SA-MXene	1.4	1000	58.77 at 5 mV s^{-1}	17.5	47.2	This work
				11.3	66.8	
				3.5	109.6	

were conducted. The XRD spectra of 12-SA-MXene were investigated during a constant-current charging/discharging process at a current density of 15 mA g^{-1}. It is shown in Fig. 5c that the peaks at 5.7°, 17.1°, and 28.7° are ascribed to the (002), (004), and (006) planes of $Ti_3C_2T_x$ MXene. During the desalination process (−1 to 1 V), the (*00l*) peaks tend to shift to higher angles gradually due to the continuous decreases in the interlayer spacing (7.8 Å to 7.5 Å based on the shift of (002)) of 12-SA-MXene, which is consistent with the desorption of Na^+. And the (*00l*) peaks shift back to the original position during the salination process from 1 V to −1 V, as a result of Na^+ intercalation between SA-MXene layers. Through the result of *in situ* XRD, the change in interlayer spacing in SA-MXene was observed during galvanostatic charging and discharging, demonstrating reversible insertion and extraction of Na^+ in the interlayer spacing of SA-MXene.

Long-term stability was studied by the cycling test (Fig. 5d). The retention of salt adsorption capacity improved from 65% to 100% for 12-SA-MXene, over 80 cycles, suggesting reliable long-term reversible desalination processes. Fig. S15† compares XPS peak fittings for pristine MXene nanosheets and 12-SA-MXene nanosheets after CDI tests. For 12-SA-MXene, the Ti species with high oxidation states are much fewer than those of pristine MXenes, suggesting good inhibition of oxidation to endure the reversible charging/discharging cycles and strong hydraulic impact in CDI tests. In addition, in the O 1s XPS spectra of SA-MXene after the CDI test, the peak present at 529.7 eV can still be observed, which represents the Ti–O–Ti bond. This demonstrates that the SA used to modify MXenes does not completely desorb due to the charging and discharging process when undergoing the CDI test. Moreover, 12-SA-MXene demonstrated an outstanding average salt adsorption rate (ASAR). Fig. S16† shows the trade-off between the ASAR and SAC of pristine and SA-modified MXene in a Ragone plot (or a Kim-Yoon plot), in which 12-SA-MXene demonstrates an outstanding desalination rate and capacity. The maximum ASAR of 12-SA-MXene reaches 17.5 mg g^{-1} min^{-1}. Such results demonstrate the remarkable potential of 12-SA-MXene in CDI technology compared to other materials in relevant literature in Table 1, which is amongst the top class of MXene-based CDI electrode materials (Fig. 5e).

To further confirm the functionality of SA modification in SA-MXene, density functional theory (DFT) calculation was performed to investigate the structural arrangement, binding affinity, and migration energy barrier for pristine MXenes and SA-MXene (Fig. 6). Fig. 6a and S17† present the favorable adsorption configuration between Na/Cl and electrode materials. As revealed, the SA-modified MXene exhibits adsorption energies towards Na and Cl of −1.13 and −1.46 eV, respectively, which are lower than those of pristine $Ti_3C_2T_x$ MXene (−0.59 and −0.72 eV, respectively). The lower adsorption energies of SA-MXene towards Na and Cl suggest that the ascorbate ion can effectively enhance the interaction between the target ions and SA-MXene which benefits the salt adsorption ability. Then, the diffusion energy barriers of Na and Cl were calculated for pristine and SA-modified MXene (Fig. 6c and d), presenting a boosted ion diffusion kinetics. The results theoretically verify the enhanced Na and Cl diffusion kinetics by the expanded interlayer spacing of SA-MXene. The coordination interaction

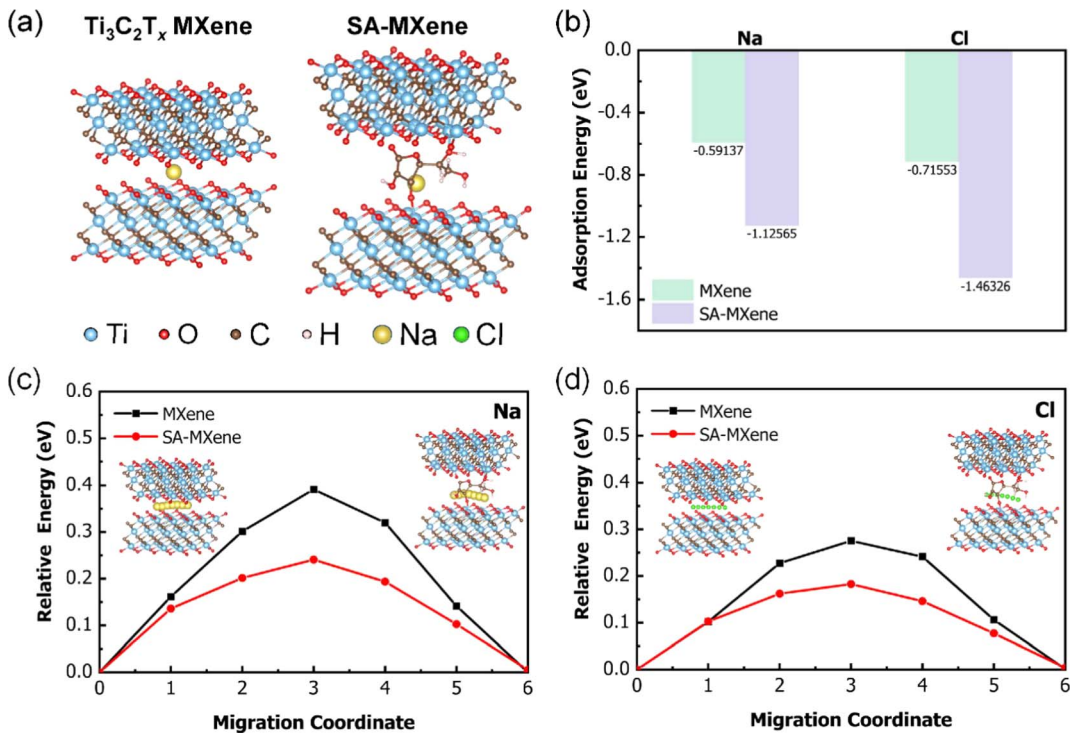

Fig. 6 Adsorption mechanism investigation. (a) Adsorption configuration of Na on the surface of $Ti_3C_2T_x$ MXene and SA-MXene. (b) Comparison of adsorption energies of Na and Cl for MXenes and SA-MXene. Relative energies of (c) Na migration and (d) Cl migration in MXenes and SA-MXene. Insets present the migration paths of Na and Cl.

between ascorbate ions and $Ti_3C_2T_x$ contributes to a higher Na/Cl adsorption and a fast Na/Cl diffusion pathway. The synergistic effect of SA-MXene results in the improvement of electrochemical behavior and desalination performance.

3 Conclusions

In summary, the SA-modified $Ti_3C_2T_x$ MXene has been successfully prepared and demonstrated enhanced desalination capacity and long-term stability. The improved performance is ascribed to the capping of MXene nanosheet edges *via* Ti–O coordination with ascorbate ions and the enlarged interlayer spacing of MXenes by the intercalation of sodium and ascorbate ions. As a result, the concentration of MXenes remains at 92% after 90 days of storage under ambient conditions, reflecting its remarkable oxidation stability. The interlayer spacing is 20% larger than that of pristine MXenes, ensuring fast ion adsorption and transfer. The synergistic effect of SA-MXene facilitates the salt adsorption process and improves its structural stability simultaneously. With the optimal ratio of SA and MXenes, the 12-SA-MXene delivered the best CDI performance, which reaches 109.6 mg g^{-1} at 1.6 V and a concentration of 750 mg L^{-1} for the NaCl feed solution. This study proposed a simple yet effective strategy to design MXene-based electrodes with high oxidation resistance for capacitive deionization and other applications in aqueous or highly humid environments.

4 Experimental

4.1 Materials

Titanium aluminum carbide (Ti_3AlC_2, MAX) was purchased from 11 Technology Co., Ltd (Jilin, China). Lithium fluoride (LiF, >99%) was purchased from Shanghai Aladdin Biochemical Technology Co., Ltd (Shanghai, China). Hydrochloric acid (HCl, 36–38%) was purchased from Shanghai Lingfeng Chemical Reagent Co., Ltd (Shanghai, China). Sodium L-ascorbate (98%) was purchased from Sigma-Aldrich (St. Louis, MO, USA).

4.2 Preparation of $Ti_3C_2T_x$ MXene

The preparation of $Ti_3C_2T_x$ MXene by etching Al in Ti_3AlC_2 MAX is a widely used method.[77] In detail, 1 g of MAX powder was slowly added to a mixture containing 3 g of LiF and 40 mL of hydrochloric acid solution (9 M), followed by stirring at 400 rpm for 24 hours at 35 °C. Then, the solid product was repeatedly washed by centrifugation at 8000 rpm for 5 minutes each time using deionized (DI) water until the pH of the product changed to 6. Afterwards, 60 mL of DI water was added to the cleaned product and treated for 30 minutes in an ice water bath under argon gas using ultrasonic apparatus. Finally, centrifugation was carried out in a centrifuge at 3000 rpm for 20 minutes. The supernatant obtained after centrifugation was a dispersion of MXene nanosheets at a concentration of 14.65 mg mL^{-1}.

4.3 Preparation of SA-modified MXene

As the amount of modification material affects the performance of the resulting materials, different concentrations of SA have been used to explore the optimum amount. First, 10 mL of MXene dispersion (146.5 mg MXene in 10 mL DI water) was added to 30 mL of SA solution at concentrations of 8, 12, and 16 mM, respectively, and stirred for 1 hour at 400 rpm in an argon stream. The resulting SA-MXene dispersion was then sonicated in an argon stream for 30 minutes. The concentration of the modified MXene dispersion can be calculated according to the following equation.

$$c_{\text{MXene in SA-MXene dispersion}} = \frac{c_{\text{MXene in pure MXene dispersion}} V_{\text{MXene dispersion}}}{V_{\text{SA solution}} + V_{\text{MXene dispersion}}} \quad (1)$$

where $c_{\text{MXene in pure MXene dispersion}}$ is 14.65 mg mL^{-1}, $V_{\text{MXene dispersion}}$ is 10 mL, and $V_{\text{SA solution}}$ is 30 mL. Thus, $c_{\text{MXene in SA-MXene dispersion}}$ can be calculated to be 3.66 mg mL^{-1}. To determine the SA to MXene ratios of SA-MXene modified using different concentrations of SA solutions, 5 mL of the SA-MXene dispersion was filtered and weighed, and a calculation was carried out according to the following equation.

$$\text{wt\%} = \frac{m_{\text{SA-MXene after filtration}} - c_{\text{MXene in SA-MXene dispersion}} V_{SA-MXene\ dispersion}}{c_{\text{MXene in SA-MXene dispersion}} V_{\text{SA-MXene dispersion}}} \quad (2)$$

The calculations resulted in SA to MXene ratios of SA-MXene of 10.9 wt%, 16.4 wt% and 21.8 wt% in 8-SA-MXene, 12-SA-MXene and 16-SA-MXene, respectively.

4.4 Preparation of CDI electrodes

To prepare the electrodes used in the CDI test, the 2 mL stable dispersions of MXene, 8 mM SA modified MXene (8-SA-MXene), 12 mM SA modified MXene (12-SA-MXene) and 16 mM SA modified MXene (16-SA-MXene) were collected by vacuum filtration, respectively, with a sintered glass filter using polyvinylidene difluoride (PVDF) membranes (0.22 μm, Merck Millipore Ltd) to obtain free-standing MXene electrodes.

4.5 Characterization

To observe the surface morphology and material structure of all samples, transmission electron microscope (TEM) images of all the samples were obtained using an FEI G2 F30 transmission electron microscope. An X-Ray diffractometer (XRD) Bruker AXS D8 Venture was used to determine the crystal structure and composition of the samples using Cu Kα radiation ($\lambda = 1.5406$ Å, 40 kV, and 40 mA). *In situ* XRD was carried out by using a Malvern Panalytical X-ray diffractometer for 12-SA-MXene, which was connected to a multichannel battery testing system (Neware) for a galvanic charging and discharging process at a current density of 30 mA g^{-1}. X-ray photoelectron spectroscopy (Thermo Scientific K-Alpha), Fourier transform infrared spectroscopy (Agilent Cary 630) and ultraviolet/visible spectroscopy (Agilent Cary 300) were used to characterize the chemical structures and chemical contents of the SA-MXene samples. X-ray photoelectron spectroscopy (XPS) was used to investigate the type of functional groups on the surface of the samples using a Thermo Scientific K-

Alpha. The ultraviolet visible (UV-vis) spectra were recorded to determine the concentration of MXenes in solution using an Agilent Cary 300 ultraviolet spectrophotometer. For electrochemical property analysis, the as-prepared electrodes were studied using a three-electrode system with Ag/AgCl as the reference electrode, and a platinum electrode as the counter electrode in 1 M NaCl solution as the electrolyte. Cyclic voltammetry (CV) and electrochemical impedance spectroscopy (EIS) were carried out using a Metrohm AUT302N potentiostatic/galvanostatic Autolab electrochemical workstation. For the CV tests, the scan rates applied were 5–100 mV s^{-1} in a potential range from 0.5 to −0.5 V. For the calculation of specific capacitance, eqn (3) given below was used.[78]

$$C_p = \frac{A}{2mk(V_2 - V_1)} \quad (3)$$

In this equation, C_p stands for the specific capacitance. A is the area surrounded by the CV curve. M is the mass of the material that is being tested. K is the scan rate in units of V s^{-1}. $(V_2–V_1)$ is the range of the scanning voltage, which is equal to 1 V in the experiment.

For EIS tests, the frequencies applied were 0.01–10,000 Hz, with a sinusoidal amplitude of 5 mV.

4.6 Setup of the CDI equipment

To evaluate the performance of electrodes in CDI technology, self-assembled CDI equipment was used in the experiment. The equipment was consisted of a peristaltic pump (BT00S, Lead Fluid), a conductivity meter (DDSJ-318F, Leici), a CDI cell with a 1 : 1 mass ratio of the cathode and anode, and a constant voltage supplier (Keithley, SMU2400). The ion-exchange membranes used in yjr CDI cell were bought from Hangzhou Iontech Environmental Technology Co., Ltd (Zhejiang, China), and the size of the CDI cell was 10 cm × 10 cm. Sodium chloride solution (40 mL) was used as the feed solution with initial concentrations of 250, 500 and 750 mg L^{-1}, and the fluid flow rate was 30 mL min^{-1}. The voltage applied to the CDI cell was varied from 1 V to 1.6 V in 0.2 V increments. The computer recorded the value of the conductivity of the NaCl solution every 10 seconds.

The salt adsorption capacity (SAC) and energy consumption of electrodes during the CDI test can be calculated according to eqn (4).[36]

$$SAC = \frac{M_w \times \int (C_i - C_0)\phi dt}{M_e} \quad (4)$$

In this equation, M_w stands for the molecular weight of the molecule to be removed. C_i is the initial concentration of the feed solution, while C_0 is its final concentration when it flows out. Φ is the flow rate of liquid and M_e means the total mass of electrodes.

4.7 Theoretical computation

The Vienna *ab initio* simulation package (VASP)[79,80] was employed to perform all the spin-polarized DFT calculations within the generalized gradient approximation (GGA) in the PBE[81] formulation. We have chosen the projected augmented wave (PAW) potentials[82,83] to describe the ionic cores and take valence electrons into account using a plane wave basis set with a kinetic energy cutoff of 450 eV. Partial occupancies of the Kohn–Sham orbitals were allowed using the Methfessel–Paxton smearing method and a width of 0.10 eV. The electronic energy was considered self-consistent when the energy change was smaller than 10^{-6} eV. A geometry optimization was considered convergent when the residual forces were smaller than 0.05 eV $Å^{-1}$. The transition state of an elementary reaction step was located by the nudged elastic band (NEB) method.[84] In the NEB method, the path between the reactant(s) and product(s) was discretized into a series of five structural images. The intermediate structures were relaxed until the perpendicular forces were smaller than 0.05 eV $Å^{-1}$. Finally, the adsorption energies (E_{ads}) were calculated as $E_{ads} = E_{ad/sub} - E_{ad} - E_{sub}$, where $E_{ad/sub}$, E_{ad}, and E_{sub} are the total energies of the optimized adsorbate/substrate system, the adsorbate in the structure, and the clean substrate, respectively.

Author contributions

C. Huang: methodology, characterization, data analysis, writing original draft. W. Zhou: methodology, characterization. X. Li: characterization, data analysis, writing – review & editing. T. Huang: visualization. M. Ding: conceptualization, supervision, writing – review & editing, funding resources.

Conflicts of interest

There are no conflicts to declare.

Acknowledgements

This work was supported by the Jiangsu Science and Technology Programme (BK20220286), the Natural Science Foundation of the Jiangsu Higher Education Institutions of China (22KJB430042), the Suzhou Science and Technology Development Planning Programme (ZXL2023195), the National Natural Science Foundation of China (22308282), and the Xi'an Jiaotong-Liverpool University's Postgraduate Research Scholarship Fund (PGRS2206051). The authors sincerely thank H. Y. Yang from the Singapore University of Technology and Design for assistance with structural and electrochemical studies.

References

1 P. Liu, T. Yan, L. Shi, H. S. Park, X. Chen, Z. Zhao and D. Zhang, *J. Mater. Chem. A*, 2017, **5**, 13907–13943.
2 K. X. Tang, T. Z. X. Hong, L. M. You and K. Zhou, *J. Mater. Chem. A*, 2019, **7**, 26693–26743.
3 Z. H. Huang, Z. Y. Yang, F. Y. Kang and M. Inagaki, *J. Mater. Chem. A*, 2017, **5**, 470–496.
4 Y. T. Cheng, Z. Q. Hao, C. R. Hao, Y. Deng, X. Y. Li, K. X. Li and Y. B. Zhao, *RSC Adv.*, 2019, **9**, 24401–24419.

5 Q. L. Liu, X. Q. Li and D. Xiao, *J. Environ. Sci. Water Resour.*, 2022, **8**, 1938–1953.
6 L. Chang, Y. H. Fei and Y. H. Hu, *J. Mater. Chem. A*, 2021, **9**, 1429–1455.
7 E. Y. Liu, L. Y. Lee, S. L. Ong and H. Y. Ng, *Water Res.*, 2020, **183**, 116059.
8 W. L. Xing, J. Liang, W. W. Tang, D. He, M. Yan, X. X. Wang, Y. Luo, N. Tang and M. Huang, *Desalination*, 2020, **482**, 114390.
9 X. Xu, M. Eguchi, Y. Asakura, L. Pan and Y. Yamauchi, *Energy Environ. Sci.*, 2023, **16**, 1815–1820.
10 Z. Xing, X. Xuan, H. Hu, M. Li, H. Gao, A. Alowasheeir, D. Jiang, L. Zhu, Z. Li, Y. Kang, J. Zhang, X. Yi, Y. Yamauchi and X. Xu, *Chem. Commun.*, 2023, **59**, 4515–4518.
11 L. Guo, R. W. Mo, W. H. Shi, Y. X. Huang, Z. Y. Leong, M. Ding, F. M. Chen and H. Y. Yang, *Nanoscale*, 2017, **9**, 13305–13312.
12 W. H. Shi, X. Y. Liu, T. Q. Deng, S. Z. Huang, M. Ding, X. H. Miao, C. Z. Zhu, Y. H. Zhu, W. X. Liu, F. F. Wu, C. J. Gao, S. W. Yang, H. Y. Yang, J. N. Shen and X. H. Cao, *Adv. Mater.*, 2020, **32**, 1907404.
13 J. Wu, X. Xuan, S. Zhang, Z. Li, H. Li, B. Zhao, H. Ye, Z. Xiao, X. Zhao, X. Xu, X. Liu, J. You and Y. Yamauchi, *Chem. Eng. J.*, 2023, **473**, 145421.
14 Y. Liu, C. Nie, L. Pan, X. Xu, Z. Sun and D. H. Chua, *Inorg. Chem. Front.*, 2014, **1**, 249–255.
15 M. Kim, H. Lim, X. Xu, M. S. A. Hossain, J. Na, N. N. Awaludin, J. Shah, L. K. Shrestha, K. Ariga, A. K. Nanjundan, D. J. Martin, J. G. Shapter and Y. Yamauchi, *Microporous Mesoporous Mater.*, 2021, **312**, 110757.
16 X. Liu, X. Xu, X. Xuan, W. Xia, G. Feng, S. Zhang, Z.-G. Wu, B. Zhong, X. Guo, K. Xie and Y. Yamauchi, *J. Am. Chem. Soc.*, 2023, **145**, 9242–9253.
17 Y. Huang, F. Chen, L. Guo and H. Y. Yang, *J. Mater. Chem. A*, 2017, **5**, 18157–18165.
18 B. Han, G. Cheng, Y. K. Wang and X. K. Wang, *Chem. Eng. J.*, 2019, **360**, 364–384.
19 Y. Liu, C. Y. Nie, X. J. Liu, X. T. Xu, Z. Sun and L. K. Pan, *RSC Adv.*, 2015, **5**, 15205–15225.
20 I. Ihsanullah and M. Bilal, *Chemosphere*, 2022, **303**, 135234.
21 P. A. Shinde, A. M. Patil, S. Lee, E. Jung and S. C. Jun, *J. Mater. Chem. A*, 2022, **10**, 1105–1149.
22 P. Srimuk, F. Kaasik, B. Krüner, A. Tolosa, S. Fleischmann, N. Jäckel, M. C. Tekeli, M. Aslan, M. E. Suss and V. Presser, *J. Mater. Chem. A*, 2016, **4**, 18265–18271.
23 M. Ghanbari, D. Emadzadeh, W. J. Lau, H. Riazi, D. Almasi and A. F. Ismail, *Desalination*, 2016, **377**, 152–162.
24 M. Bounaas, A. Bouguettoucha, D. Chebli, J. M. Gatica and H. Vidal, *Arabian J. Sci. Eng.*, 2021, **46**, 325–341.
25 K. Maleski, V. N. Mochalin and Y. Gogotsi, *Chem. Mater.*, 2017, **29**, 1632–1640.
26 X. H. Wu, Z. Y. Wang, M. Z. Yu, L. Y. Xiu and J. S. Qiu, *Adv. Mater.*, 2017, **29**, 1607017.
27 X. J. Shen, Y. C. Xiong, R. T. Hai, F. Yu and J. Ma, *Environ. Sci. Technol.*, 2020, **54**, 4554–4563.
28 M. M. Hasan, M. M. Hossain and H. K. Chowdhury, *J. Mater. Chem. A*, 2021, **9**, 3231–3269.
29 K. Li, M. Y. Liang, H. Wang, X. H. Wang, Y. S. Huang, J. Coelho, S. Pinilla, Y. L. Zhang, F. W. Qi, V. Nicolosi and Y. X. Xu, *Adv. Funct. Mater.*, 2020, **30**, 2000842.
30 Z. G. Hao, S. H. Zhang, S. Yang, X. Y. Li, Y. J. Gao, J. Peng, L. J. Li, L. X. Bao and X. Li, *ACS Appl. Energy Mater.*, 2022, **5**, 2898–2908.
31 V. Natu, J. L. Hart, M. Sokol, H. Chiang, M. L. Taheri and M. W. Barsoum, *Angew. Chem., Int. Ed.*, 2019, **58**, 12655–12660.
32 X. Yang, Y. Yao, Q. Wang, K. Zhu, K. Ye, G. Wang, D. Cao and J. Yan, *Adv. Funct. Mater.*, 2021, **32**, 2109479.
33 Y. Li, K. Wu, M. Zhang, X. Yang, W. Feng, P. Wang, K. Li, Y. Zhan and Z. Zhou, *Ceram. Int.*, 2022, **48**, 37032–37038.
34 Y. M. Cai, W. Zhang, J. S. Zhao and Y. Wang, *Appl. Surf. Sci.*, 2023, **622**, 156926.
35 S. H. Zhang, X. T. Xu, X. H. Liu, Q. Yang, N. Z. Shang, X. X. Zhao, X. H. Zang, C. Wang, Z. Wang, J. G. Shapter and Y. Yamauchi, *Mater. Horiz.*, 2022, **9**, 1708–1716.
36 X. F. Zhao, A. Vashisth, E. Prehn, W. M. Sun, S. Shah, T. Habib, Y. X. Chen, Z. Y. Tan, J. Lutkenhaus, M. Radovic and M. J. Green, *Matter*, 2019, **1**, 513–526.
37 C.-W. Wu, B. Unnikrishnan, I. W. P. Chen, S. G. Harroun, H.-T. Chang and C.-C. Huang, *Energy Storage Materials*, 2020, **25**, 563–571.
38 F. Cao, Y. Zhang, H. Wang, K. Khan, A. K. Tareen, W. Qian, H. Zhang and H. Agren, *Adv. Mater.*, 2022, **34**, e2107554.
39 B. B. Chen, A. H. Feng, R. X. Deng, K. Liu, Y. Yu and L. X. Song, *ACS Appl. Mater. Interfaces*, 2020, **12**, 13750–13758.
40 B. J. Zhang, A. Boretti and S. Castelletto, *Chem. Eng. J.*, 2022, **435**, 134959.
41 Q. Liu, X. Li, G. Tan and D. Xiao, *Desalination*, 2022, **538**, 115890.
42 P. C. F. Pau, J. O. Berg and W. G. Mcmillan, *J. Phys. Chem.*, 1990, **94**, 2671–2679.
43 X. Li, W. B. You, C. Y. Xu, L. Wang, L. T. Yang, Y. S. Li and R. C. Che, *Nano-Micro Lett.*, 2021, **13**, 157.
44 S. Chen, Y. F. Xiang, M. K. Banks, C. Peng, W. J. Xu and R. X. Wu, *Nanoscale*, 2018, **10**, 20053.
45 J. H. Wang, D. G. Jiang, M. Z. Zhang, Y. S. Sun, M. Y. Jiang, Y. Q. Du and J. Q. Liu, *J. Mater. Chem. A*, 2023, **11**, 1419–1429.
46 X. F. Zhao, D. E. Holta, Z. Y. Tan, J. H. Oh, I. J. Echols, M. Anas, H. X. Cao, J. L. Lutkenhaus, M. Radovic and M. J. Green, *ACS Appl. Nano Mater.*, 2020, **3**, 10578–10585.
47 C. W. Wu, B. Unnikrishnan, I. W. P. Chen, S. G. Harroun, H. T. Chang and C. C. Huang, *Energy Storage Materials*, 2020, **25**, 563–571.
48 Y. Liu, Y. Shi, C. Gao, Z. Shi, H. Ding, Y. Feng, Y. He, J. Sha, J. Zhou and B. Lu, *Angew. Chem., Int. Ed.*, 2023, **62**, e202300016.
49 J. Li, M. Lu, W. Zheng and W. Zhang, *Energy Storage Materials*, 2024, **64**, 103068.
50 D. Kowalczyk, W. Kazimierczak, E. Zieba, M. Mezynska, M. Basiura-Cembala, S. Lisiecki, M. Karas and B. Baraniak, *Carbohydr. Polym.*, 2018, **181**, 317–326.

51 S. Wan, X. Li, Y. Chen, N. Liu, Y. Du, S. Dou, L. Jiang and Q. Cheng, *Science*, 2021, **374**, 96–99.
52 X. Y. Wang, S. Y. Liao, H. P. Huang, Q. F. Wang, Y. Y. Shi, P. L. Zhu, Y. G. Hu, R. Sun and Y. J. Wan, *Small Methods*, 2023, **7**, 2201694.
53 F. X. Yang, Y. Huang, X. P. Han, S. Zhang, M. Yu, J. P. Zhang and X. Sun, *ACS Appl. Nano Mater.*, 2023, **6**, 9070.
54 J. L. Zhang, H. J. Yang, G. X. Shen, P. Cheng, J. Y. Zhang and S. W. Guo, *Chem. Commun.*, 2010, **46**, 1112–1114.
55 A. Ravi, M. A. Malone, A. Luthra, D. Lioi and J. V. Coe, *Phys. Chem. Chem. Phys.*, 2013, **15**, 10307–10315.
56 X. F. Zhao, A. Vashisth, J. W. Blivin, Z. Y. Tan, D. E. Holta, V. Kotasthane, S. A. Shah, T. Habib, S. H. Liu, J. L. Lutkenhaus, M. Radovic and M. J. Green, *Adv. Mater. Interfaces*, 2020, **7**, 2000845.
57 M. Ding, W. H. Shi, L. Guo, Z. Y. Leong, A. Baji and H. Y. Yang, *J. Mater. Chem. A*, 2017, **5**, 6113–6121.
58 S. Fleischmann, J. B. Mitchell, R. C. Wang, C. Zhan, D. E. Jiang, V. Presser and V. Augustyn, *Chem. Rev.*, 2020, **120**, 6738–6782.
59 M. L. Wang, S. X. Feng, C. Bai, K. Ji, J. X. Zhang, S. L. Wang, Y. Q. Lu and D. S. Kong, *Small*, 2023, **19**, 2300386.
60 Y. Cai, Y. Wang, L. Zhang, R. Fang and J. Wang, *ACS Appl. Mater. Interfaces*, 2022, **14**, 2833–2847.
61 S. Zhang, X. Xu, X. Liu, Q. Yang, N. Shang, X. Zhao, X. Zang, C. Wang, Z. Wang, J. G. Shapter and Y. Yamauchi, *Mater. Horiz.*, 2022, **9**, 1708–1716.
62 S. Anwer, D. H. Anjum, S. H. Luo, Y. Abbas, B. S. Li, S. Iqbal and K. Liao, *Chem. Eng. J.*, 2021, **406**, 126827.
63 J. Ai, J. Li, K. Li, F. Yu and J. Ma, *Chem. Eng. J.*, 2021, **408**, 127256.
64 Z. Y. Tan, W. Wang, M. K. Zhu, Y. C. Liu, Y. X. Yang, X. H. Ji and Z. K. He, *Desalination*, 2023, **548**, 116267.
65 M. Torkamanzadeh, L. Wang, Y. Zhang, O. Budak, P. Srimuk and V. Presser, *ACS Appl. Mater. Interfaces*, 2020, **12**, 26013–26025.
66 H. T. Xu, M. Li, S. Q. Gong, F. Zhao, Y. Zhao, C. L. Li, J. J. Qi, Z. Y. Wang, H. H. Wang, X. B. Fan, W. C. Peng and J. P. Liu, *J. Colloid Interface Sci.*, 2022, **624**, 233–241.
67 C. X. Yao, W. Q. Zhang, L. J. Xu, M. M. Cheng, Y. Su, J. Xue, J. L. Liu and S. F. Hou, *Sep. Purif. Technol.*, 2021, **263**, 118365.
68 Y. Cai, W. Zhang, J. Zhao and Y. Wang, *Appl. Surf. Sci.*, 2023, **622**, 156926.
69 N. N. Liu, L. L. Yu, B. J. Liu, F. Yu, L. Q. Li, Y. Xiao, J. H. Yang and J. Ma, *Adv. Sci.*, 2023, **10**, 2204041.
70 K. Wang, L. Chen, G. Zhu, X. T. Xu, L. J. Wan, T. Lu and L. K. Pan, *Desalination*, 2022, **522**, 115420.
71 Z. Q. Chen, X. T. Xu, Y. Liu, J. F. Li, K. Wang, Z. B. Ding, F. Y. Meng, T. Lu and L. K. Pan, *Desalination*, 2022, **528**, 115616.
72 S. Buczek, M. L. Barsoum, S. Uzun, N. Kurra, R. Andris, E. Pomerantseva, K. A. Mahmoud and Y. Gogotsi, *Energy Environ. Mater.*, 2020, **3**, 398–404.
73 X. Shen, Y. Xiong, R. Hai, F. Yu and J. Ma, *Environ. Sci. Technol.*, 2020, **54**, 4554–4563.
74 J. Ma, Y. Cheng, L. Wang, X. Dai and F. Yu, *Chem. Eng. J.*, 2020, **384**, 123329.
75 X. Shen, R. Hai, X. Wang, Y. Li, Y. Wang, F. Yu and J. Ma, *J. Mater. Chem. A*, 2020, **8**, 19309–19318.
76 M. Ding, S. Li, L. Guo, L. Jing, S.-P. Gao, H. Yang, J. M. Little, T. U. Dissanayake, K. Li, J. Yang, Y.-X. Guo, H. Y. Yang, T. J. Woehl and P.-Y. Chen, *Adv. Energy Mater.*, 2021, **11**, 2101494.
77 M. M. Baig, I. H. Gul, S. M. Baig and F. Shahzad, *J. Electroanal. Chem.*, 2022, **904**, 115920.
78 C. Mondal, D. Ghosh, T. Aditya, A. K. Sasmal and T. Pal, *New J. Chem.*, 2015, **39**, 8373–8380.
79 G. Kresse and J. Furthmuller, *Comput. Mater. Sci.*, 1996, **6**, 15–50.
80 G. Kresse and J. Furthmuller, *Phys. Rev. B: Condens. Matter Mater. Phys.*, 1996, **54**, 11169–11186.
81 J. P. Perdew, K. Burke and M. Ernzerhof, *Phys. Rev. Lett.*, 1996, **77**, 3865–3868.
82 G. Kresse and D. Joubert, *Phys. Rev. B: Condens. Matter Mater. Phys.*, 1999, **59**, 1758–1775.
83 P. E. Blochl, *Phys. Rev. B: Condens. Matter Mater. Phys.*, 1994, **50**, 17953–17979.
84 G. Henkelman, B. P. Uberuaga and H. Jónsson, *J. Chem. Phys.*, 2000, **113**, 9901–9904.